A wave data assimilation system for the North Sea based on Ensemble Kalman Filtering and the potential of satellite altimetry

de Korte, C. W.E.; Verlaan, M.; Heemink, A. W.

DOI
10.1016/j.ocemod.2025.102586

Publication date
2025

Document Version
Final published version

Published in
Ocean Modelling

Citation (APA)
de Korte, C. W. E., Verlaan, M., & Heemink, A. W. (2025). A wave data assimilation system for the North Sea based on Ensemble Kalman Filtering and the potential of satellite altimetry. *Ocean Modelling*, *197*, Article 102586. https://doi.org/10.1016/j.ocemod.2025.102586

Ocean Modelling 197 (2025) 102586

Contents lists available at ScienceDirect

Ocean Modelling

journal homepage: www.elsevier.com/locate/ocemod

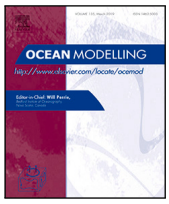

A wave data assimilation system for the North Sea based on Ensemble Kalman Filtering and the potential of satellite altimetry

C.W.E. de Korte [a,b,*], M. Verlaan [a,b], A.W. Heemink [a]

[a] Technische Universiteit Delft, Mekelweg 4, Delft, 2628 CD, Zuid-Holland, Netherlands
[b] Deltares, Boussinesqweg 1, Delft, 2629 HV, Zuid-Holland, Netherlands

ARTICLE INFO

Dataset link: https://github.com/OpenDA-Association, https://gitlab.tudelft.nl/citg/wavemodels/swan, https://doi.org/10.48670/moi-00179

Keywords:
Wave data assimilation
Ensemble Kalman Filter
Identical twin experiment
Satellite altimetry

ABSTRACT

A Wave Data Assimilation System based on the Ensemble Kalman Filter (EnKF) is implemented for the North Sea showing improved performance and physical consistency. We first show the EnKF implementation and illustrate the wave data assimilation system using identical twin experiments to assimilate synthetic observations from buoys. A sensitivity analysis shows that the ensemble size, assimilation frequency and observation uncertainty are relatively important settings. Lastly, the potential for assimilating satellite measurements was assessed by assimilating synthetic altimeter measurements with real pass-over tracks. In these experiments, the state contains the full wave spectrum, unlike in most existing schemes. The results show that wave spectra and integral variables beyond significant wave height show physically consistent updates for the buoy and satellite experiments, by assimilating only significant wave height. This is a key advantage of this implementation compared to the more widely used implementations in wave data assimilation. Although the satellite experiment performs slightly worse than the buoy experiment due to decreased temporal availability of measurements, the results underline the potential for assimilation of satellite altimeter measurements. Such a system provides a promising framework for future observation impact study using satellite altimeter measurements.

1. Introduction

Wave hindcasting and forecasting are important for a better understanding of ocean and climate processes, early coastal warning systems, shipping and offshore engineering. Wave models continue to face limitations, particularly in coastal shelf seas, where uncertainties persist regarding wave–current interactions, wind forcing, and wave-bottom interactions (Cavaleri et al., 2018). Satellite altimeters continue to have global coverage since 1985 (Ribal and Young, 2019), while satellite processing techniques are advancing (e.g., Tourain et al., 2021; Schlembach et al., 2023). Satellite measurements and wave models are two sources of information that can be integrated. Data assimilation (DA) leverages both model physics and measurement data by using knowledge of wave dynamics and observations to more accurately estimate the true wave state. Reanalyses (data assimilated products) are nowadays often considered the best source of training data for deep learning models. For example, the purely data-driven forecast model GraphCast (Google) is trained on 1979–2017 ERA5 reanalysis data (Lam et al., 2022). Similarly, ECMWF has deployed an Artificial Intelligence integrated forecasting system (AIFS), trained on ERA5 reanalysis data (Lang et al., 2024). Hence, the importance of (partly) physics-based modelling remains.

Early studies on wave DA date back to the eighties, with attempts by Esteva (e.g., 1988), Janssen et al. (e.g., 1989) and Lionello et al. (e.g., 1995). These approaches used Optimal Interpolation schemes (OI). Others developed variational implementations using an adjoint (De Las Heras et al., 1994). The development continued with approaches using spectral partitioning to assimilate spectral wave data (Voorrips et al., 1997; Hasselmann et al., 1997). Kalman Filter methods were applied for the first time in wave DA by Voorrips et al. (1999). More recently, implementations of 4DVAR schemes (four-dimensional variational) (Song and Mayerle, 2017), 3DVAR schemes (three-dimensional variational) (Saulter et al., 2020), the Ensemble Kalman Filter (EnKF) (Almeida et al., 2016; Caires et al., 2018b,a; Kim et al., 2020) and the Local Ensemble Transform Kalman Filter (LETKF) (Houghton et al., 2023) have been published. Even though the OI scheme dates back to the eighties, the relatively simple and fast OI scheme remains prominent in wave DA until today, (e.g., Skandrani et al., 2004; Aouf et al., 2006; Yu et al., 2018; Li and Zhang, 2020; Smit et al., 2021; Houghton et al., 2022; Wang et al., 2024). Most

* Corresponding author at: Technische Universiteit Delft, Mekelweg 4, Delft, 2628 CD, Zuid-Holland, Netherlands.
E-mail address: eliasdekorte@tudelft.nl (C.W.E. de Korte).

https://doi.org/10.1016/j.ocemod.2025.102586
Received 1 December 2024; Received in revised form 6 June 2025; Accepted 17 June 2025
Available online 30 June 2025

operational forecasting centres still use the OI scheme, as pointed out by Houghton et al. (2022). Assimilating satellite wave measurements has been mainly done in global context, which raises the question of the added benefit of satellite measurements in coastal shelf seas like the North Sea. An exception for the North Sea using 3DVAR and satellite measurements has been published by Saulter et al. (2020). To date, an EnKF based wave DA system using satellite data for the North Sea does not exist, and other shelf sea implementations are scarce.

Most existing schemes (e.g., OI, 3DVAR) have three main difficulties that we aim to overcome with an EnKF implementation. The EnKF is based on the Kalman Filter (Kalman, 1960) and it was developed by Evensen (1994). A conceptual overview of the EnKF and an implementation routine can be found in Evensen (2004).

In wave DA, the first difficulty is that usually the initial conditions are considered as control variables. This means that updates could be neutralized by the wind forcing in the next step, in particular in wind-wave dominated seas. Saulter et al. (2020) and Houghton et al. (2023) recommend moving towards coupled systems to advance wave DA performance. We take an intermediate approach similar to Caires et al. (2018a,b) and Kim et al. (2020), by using the EnKF and setting the wind forcing as control. A noise model is used to model the uncertainty in the wind fields. By means of the ensemble, the covariance between wind and wave fields is calculated. Corrections to the waves are made indirectly through the wind fields and the energy balance can evolve naturally.

The second drawback of existing schemes is that assumptions are made about the shape of the wave spectrum because H_s is used as the state variable. By taking the directional wave spectrum as the state variable, these assumptions are omitted. This allows us to study how corrections based on H_s observations translate to the directional wave spectrum and other integral variables like mean wave direction and mean wave period.

Thirdly, existing schemes often require prescribed error covariances that might lack realistic dynamic system error estimates as a consequence. Ensemble methods provide an effective alternative by modelling uncertainty dynamically through the ensemble statistics.

Despite the fact that these approaches combined increase the computational burden compared to the existing schemes, which may result in them not being operationally feasible, using them to create accurate reanalyses to train AI/ML models, or improving the efficiency at a later stage, could in the future support operational forecasting. The main aim of this study is to assess the potential information and physical consistency of the EnKF implementation and the potential of satellite altimeter observations. The study prepares the methods and setup for an Observing System Experiment (OSE).

The wave model is introduced in Section 2. Next, we explain how the model can be represented in state space in Section 3. From this, the conceptual formulation of the EnKF and implementation details naturally follow, in Section 4. Consequently, the identical twin experiments are introduced followed by the storm case study with the model input (Sections 5 and 6). Results are then presented for synthetic buoys (Section 7), a sensitivity study (Section 8) and finally synthetic altimeter measurements (Section 9). We end with a discussion and conclusion in Sections 10 and 11.

2. Wave model SWAN

Simulating WAves Nearshore (SWAN) (Booij et al., 1999) is a third-generation spectral wave model for shallow water that models the evolution of the wave spectrum according to the action balance equation (Eq. (1)). For this study, SWAN version 41.45 was used. The evolution of the spectrum is modelled according to action density N in space and time. The typical model output is in the form of the energy density $E(\sigma,\theta)$, where σ refers to the radian frequency over which energy is distributed and θ the spatial direction. Action density, N, equals E/σ. The rate of change of N in geographical space $(\vec{x};\sigma,\theta)$ can be described by the action balance equation (Komen, 1994) (Eq. (1)).

$$\frac{\partial N}{\partial t} + \nabla_{\vec{x}} \cdot \left[(\vec{c}_g + \vec{u})N\right] + \frac{\partial c_\sigma N}{\partial \sigma} + \frac{\partial c_\theta N}{\partial \theta} = \frac{S_{\text{tot}}}{\sigma} \tag{1}$$

On the left-hand side, The second term, $\nabla_{\vec{x}} \cdot \left[(\vec{c}_g + \vec{u})N\right]$ describes the propagation of wave energy in geographical space, with wave group velocity $\vec{c}_g = \partial\sigma/\partial\vec{k}$. The third term, $\partial c_\sigma N/\partial\sigma$, represents the shift of wave energy between radian frequencies caused by variations in mean currents and water depth. The fourth term, $\partial c_\theta N/\partial\theta$, models refraction by bottom topography and current variations. S_{tot} is the source and sink term including all processes that put energy in, redistribute or dissipate. This term comprises wind input, wave dissipation through wave breaking and nonlinear wave interactions (triads and quadruplets). These terms can be controlled with SWAN-specific settings. SWAN state variables are expressed as energy density or variance density $E(\sigma,\theta)$, not as action density.

3. State space representation of the model

Most spectral wave models contain the full wave energy density spectrum as the model state. A reduced state containing significant wave height (H_s) and peak period (T_p) is computationally more efficient but lacks realistic wave energy updates (Voorrips et al., 1999). Here, the model state contains the wave energy spectrum for 36 frequencies and 32 directional bins for the entire spatial grid ($21 \times 27 = 567$). The model state vector thus has a length of $32 \times 36 \times 567 = 653\,184$. As mentioned, note that a limitation of other methods used in wave DA like OI and 3DVAR, is that corrections are made in terms of observation values in significant wave height, H_s (e.g., Saulter et al. (2020), and Houghton et al. (2022) for 3DVAR and OI respectively). An ad hoc step is required to scale back H_s to the full wave energy spectrum. This is bound to make simplified assumptions on the sea state. This can be avoided by taking the full directional wave spectrum as model state variable.

Let $\mathbf{x}(t_{k-1}) \in \mathbb{R}^n$ be the state vector that represents the state of the system at discrete time $k-1$:

$$\mathbf{x}(t_{k-1}) = [x_1(t_{k-1}), x_2(t_{k-1}), \ldots, x_n(t_{k-1})]^T \tag{2}$$

In this case, the state vector contains the energy density wave spectrum, $E(\sigma,\theta)$.

Let $M : \mathbb{R}^n \to \mathbb{R}^n$ denote the mapping of the state space or the nonlinear model. That is, $M(\mathbf{x}) = \left(M_1(\mathbf{x}), M_2(\mathbf{x}), \ldots, M_n(\mathbf{x})\right)^T$ is a vector function of the vector $\mathbf{x}$. The evolution of the state of the dynamic system can then be described as:

$$\mathbf{x}(t_k) = M(\mathbf{x}(t_{k-1}), t_{k-1}) \tag{3}$$

To represent model errors or uncertainty in the system an additional term is added (randomness can be introduced by initial conditions, model forcing or model parameters). The stochastic model equation can be represented as:

$$\mathbf{x}(t_k) = M(\mathbf{x}(t_{k-1}), t_{k-1}) + \mathbf{w}(t_{k-1}) \tag{4}$$

with dynamic system noise as white Gaussian noise with $\mathbf{w}(t_k) \sim \mathcal{N}(0, \mathbf{Q}_k)$. The measurements $\mathbf{z}(t_k)$ are assumed to be a linear function of the state:

$$\mathbf{z}(t_k) = \mathbf{H}\mathbf{x}(t_k) + \mathbf{v}(t_k) \tag{5}$$

with $\mathbf{H}$ as the measurement operator that maps the observations to the model state and $\mathbf{v}(t_k)$ as white Gaussian observation noise with $\mathbf{v}(t_k) \sim \mathcal{N}(0, \mathbf{R}_k)$. Here we assume a linear measurement operator, but later we will explain how to deal with a nonlinear measurement operator. Illustrative for the measurement operator in this case, is that wave measurements are often given in significant wave height H_s and have to be mapped to the model state that is represented in terms of the energy density spectrum $E(\sigma,\theta)$.

4. Ensemble Kalman Filter (EnKF)

The EnKF approximates the model uncertainty represented by $\mathbf{w}(t_{k-1})$ in Eq. (4) by means of an ensemble of perturbed states (Evensen, 2004). This is part of the forecast step in the first part of the EnKF. In the second step, the analysis, a best estimate is made by using a weight matrix to minimize the variance between measurement and model.

More precisely, consider an initial ensemble $\boldsymbol{\xi}_i^a(t_0)$ to compute the wave model state sequentially in time with nonlinear model operator M for each ensemble member i to N and generate a forecast for each member $\boldsymbol{\xi}_i^f$ at t_k:

$$\boldsymbol{\xi}_i^f(t_k) = M(\boldsymbol{\xi}_i^a(t_{k-1}), t_{k-1}) + \mathbf{w}_i(t_{k-1}) \tag{6}$$

where $\boldsymbol{\xi}_i^a(t_{k-1})$ denotes the analysis member at time t_{k-1} and $w_i(t_{k-1})$ represents the system noise. The ensemble mean $\hat{\mathbf{x}}^f(t_k)$ is then given by:

$$\hat{\mathbf{x}}^f(t_k) = \frac{1}{N}\sum_{i=1}^{N} \boldsymbol{\xi}_i^f(t_k) \tag{7}$$

and the forecast error $\boldsymbol{e}_i^f(t_k)$ by:

$$\boldsymbol{e}_i^f(t_k) = \boldsymbol{\xi}_i^f(t_k) - \hat{\mathbf{x}}^f(t_k) \tag{8}$$

The ensemble model error covariance $\mathbf{P}^f(t_k)$ is given by:

$$\mathbf{P}^f(t_k) = \frac{1}{N-1}\sum_{i=1}^{N} \left[\boldsymbol{e}_i^f(t_k)\right]\left[\boldsymbol{e}_i^f(t_k)\right]^T \tag{9}$$

Eqs. (6)–(9) are called the forecast step in DA. The analysis or measurement step essentially minimizes the variance between observations $\mathbf{z}_i(t_k)$ and the transformed model state $\mathbf{H}\boldsymbol{\xi}_i^f(t_k)$. The analysis $\boldsymbol{\xi}_i^a$ at t_k is given by:

$$\boldsymbol{\xi}_i^a(t_k) = \boldsymbol{\xi}_i^f(t_k) + \mathbf{K}(t_k)\left[\mathbf{z}_i(t_k) - \mathbf{H}\boldsymbol{\xi}_i^f(t_k) - \mathbf{v}_i(t_k)\right] \tag{10}$$

where $\mathbf{v}_i(t_k)$ represents a perturbation of the observations to obtain a consistent ensemble, avoiding a too low variance (Burgers et al., 1998). We can express the Kalman Gain $\mathbf{K}(t_k)$ that represents the combined weights of measurements and model as:

$$\mathbf{K}(t_k) = \mathbf{P}^f(t_k)\mathbf{H}^T\left[\mathbf{H}\mathbf{P}^f(t_k)\mathbf{H}^T + \mathbf{R}(t_k)\right]^{-1} \tag{11}$$

where $\mathbf{H}$ denotes the linear observation operator that maps the model state to the observation measurements. Here $\mathbf{R}(t_k)$ denotes the observation error covariance matrix. After this the analysis mean $\hat{\mathbf{x}}^a(t_k)$ can be obtained:

$$\hat{\mathbf{x}}^a(t_k) = \frac{1}{N}\sum_{i=1}^{N} \boldsymbol{\xi}_i^a(t_k), \tag{12}$$

the analysis error:

$$\boldsymbol{e}_i^a(t_k) = \boldsymbol{\xi}_i^a(t_k) - \hat{\mathbf{x}}^a(t_k) \tag{13}$$

and the analysis covariance $\mathbf{P}^a(t_k)$:

$$\mathbf{P}^a(t_k) = \frac{1}{N-1}\sum_{i=1}^{N} \left[\boldsymbol{e}_i^a(t_k)\right]\left[\boldsymbol{e}_i^a(t_k)\right]^T \tag{14}$$

Note that in the actual implementation of the algorithm the computation of covariance matrices (Eqs. (9) and (14)) can be avoided (Appendix A). In the conceptual formulation, we defined a linear measurement operator and we assume that each observation is a linear combination of the model state. However, the wave measurements are often in H_s [m] and the wave model state in $E(\sigma,\theta)$ [m^2/Hz], so a nonlinear operation is needed. Appendix B shows how we linearize the observation operator. It will not always be the case that observations arrive on regular intervals on the analysis times, in particular for satellite observations. In this case, we take the ensemble of observations within the assimilation window, using the asynchronous EnKF implementation from Sakov et al. (2010). The solution is ideal for linear observations and models but provides a suboptimal solution for weak violation of the linear case. We used the open data assimilation toolbox OpenDA (version 3.1.1), which has a black box model wrapper and hosts a wide range of data assimilation algorithms (Ridler et al., 2014) (https://github.com/OpenDA-Association).

4.1. System uncertainty

In wave DA it is commonly assumed that the ocean wave state is the main source of uncertainty and therefore a perturbed wave model ensemble is often used. (Saulter et al., 2020; Houghton et al., 2022, e.g.,). This could be partially inspired by the dynamics of ocean waves, not always correlated with wind fields, its heritage in DA in meteorology where weather models are sensitive to initial conditions, or the computational expense of coupled models.

The implementation in this study is based on the assumption that the main source of system uncertainty is contained in the wind fields. The wind forcing is the so-called control variable. Wave parameters at the boundary or the initial wave state can also be considered sources of uncertainty in the system. Nonetheless, we assume that for the North Sea wind and wave fields are highly correlated most of the time. To model the uncertainty in the wind field, a stochastic first-order autoregressive process or AR(1) noise model was implemented:

$$\boldsymbol{\eta}(t_k) = a\boldsymbol{\eta}(t_{k-1}) + \mathbf{w}(t_k) \tag{15}$$

with the auto-regressive coefficient $a = \exp^{(-\frac{\Delta t}{T})}$ and $\mathbf{w}(t_k) \sim \mathcal{N}(0, \mathbf{Q}(t_k))$. Where T is the time at which the correlation becomes negligible.

The meridional and zonal wind components were treated independently. The error covariance also decays exponentially over distance. The error covariance can be described by:

$$\mathbf{Q}(t_k) = \sigma_{x_1}\sigma_{x_2}\exp^{(-\frac{\Delta x}{L})} \tag{16}$$

with σ_{x_1} and σ_{x_2} being the standard deviation of the errors at location x_1 and x_2, L the distance at which the correlation becomes negligible. Sequential algorithms like the EnKF are required to satisfy the Markov property. The property states that a stochastic process only depends on its current state and does not have 'memory' of history. The noise model in a sequential algorithm like the EnKF introduces the issue that $\mathbf{w}(t_k)$ is not independent of the previous noise term $\mathbf{w}(t_{k-1})$ through $\boldsymbol{\eta}(t_{k-1})$. This problem is solved by augmenting the state with the AR(1) forcing.

Localization is a common way in DA to limit spurious correlations as a result of finite ensemble size and possibly in combination with a large number of observations. We did not implement localization yet, because we were able to run experiments with sufficiently large ensemble sizes.

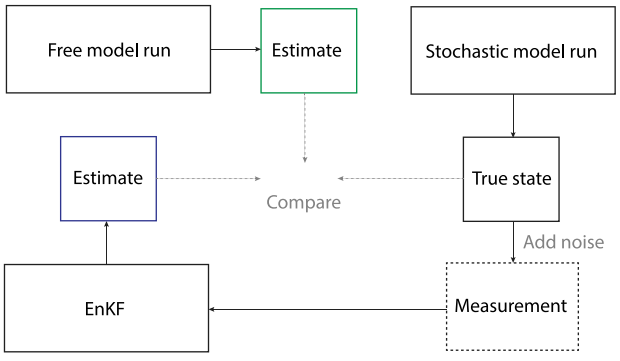

Fig. 1. Schematic overview of an identical twin experiment.

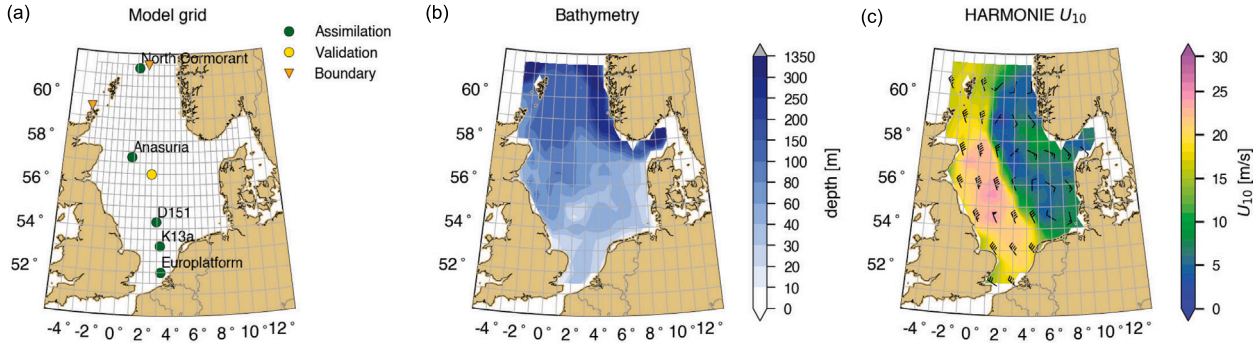

Fig. 2. (a) Model grid (0.5 by 0.5 degrees) with assimilated stations in green and the two boundary points in orange, that were used to make a uniform west and north boundary; (b) Coarsened (0.5 by 0.5 degrees) NOOS bathymetry; (c) Coarsened (0.5 by 0.5 degrees) HARMONIE input wind field at 2022-31T07:00.

5. Identical twin experiments

Identical twin experiments are a common starting point in setting up a DA system because they facilitate the assessment of the relative impact of various settings and the observations in a controlled way. Another advantage is that we have access to all variables. This is often considered a necessary step before assimilating real data. In the identical twin experiments, we created synthetic observations from the so-called truth run. This is a wave model run where the wind fields were perturbed with the noise model defined in Section 4.1. Gaussian white noise was added to the observations extracted from the truth run. We assimilate these observations with the EnKF and test how well the truth is reconstructed. Fig. 1 shows a schematic overview of an identical twin experiment. We have conducted two types of twin experiments: firstly assimilating synthetic buoy measurements to set up the wave DA system. In addition, we used the buoy experiment to conduct a sensitivity analysis to better estimate the importance of the filter settings. Secondly, we are interested in assessing the potential impact of wave altimeter measurements in this wave DA system. To this end, synthetic altimeter wave measurements with real pass-over signatures were assimilated.

6. Storm case study

For all experiments, we take a six-day period in 2022 that captured storms Malik and Corrie. This period was chosen because it has several intervals of storm growth and decay in a short time window. Consequently, the EnKF can be tested on a range of system dynamics.

Two sequential intense low-pressure fields moved over Scotland at the end of January/beginning of February 2022. Storm Malik (2022-01-28 to 2022-01-30) and Storm Corrie (2022-01-31 to 2022-02-01) crossed the North Sea in quick succession and were associated with strong north-westerly winds, with wind gusts recorded up to 120–130 km/h.

For the wind forcing HARMONIE winds were obtained from the KNMI (Royal Netherlands Meteorological Institute) with resolution 2.5 by 2.5 km. These were converted to coarse resolution (0.5 by 0.5 degrees) to match the wave model resolution. Wind fields were available every 3 h. This simplification does not impact the results of identical twin experiments but will play a role when assimilating real data.

Boundaries were taken from a nested SWAN-DCSM (Dutch Continental Shelf Model) run (Gautier and Caires, 2015). For this experiment, a uniform boundary condition across the northern and western boundaries was used for convenience in implementation. Wave parameters from the 5th point on the northern boundary and the 19th point on the western boundary were taken as representative for respectively the north and west boundary, marked in Fig. 2a. A coarse version of the NOOS (North West European Shelf Operational Oceanographic System) bathymetry (Zijderveld and Verlaan, 2004) (Fig. 2b) and DCSM-FM-100 m HARMONIE (Zijl et al., 2022) water levels were used.

To represent wind growth and white-capping, formulations from Komen et al. (1984) were used. Only quadruplets were included from wave-wave interactions. For dissipation by wave breaking, a constant breaking index was used with a proportionality coefficient for the rate of dissipation of 1, and a breaker index of 0.73. Wave dissipation by bottom friction is included with the JONSWAP semi-empirical formulation from Hasselmann et al. (1973). These are SWAN default settings.

7. Results: assimilation synthetic buoy observations

7.1. Initial settings

Assessing the impact of observations with a twin experiment requires that realistic, although not necessarily perfect values for the EnKF parameters are specified. To choose realistic first values for system uncertainty, we analysed samples of differences between different HARMONIE wind field nowcasts and a 24 h forecast for the same moment, provided by KNMI (Royal Netherlands Meteorological Institute). We approximated the error in the wind fields taking the standard deviation of the errors between nowcast and forecast. The time and distance length scales over which the error correlation becomes negligible, was approximated from the covariances of nowcast and forecast binned per distance and time.

Recall that we implemented an AR(1) noise model for the wind forcing (Eq. (15)). The error covariance decays exponentially over time and distance with a typical length and time scale. The initial values for σ_{x_1} and σ_{x_2} were set to 2 m/s and $T = 15$ h and $L = 500$ km, based on the distribution and covariance of differences between HARMONIE nowcast and forecast wind fields. Except the standard deviation of the wind noise model was taken higher to maintain sufficient ensemble spread.

For the measurement uncertainty, typical errors between model and buoy measurements were taken as representative. Based on this, a standard deviation of 0.2 m for H_s was chosen, corresponding with the true noise standard deviation of the synthetic observations.

An ensemble size of $N = 64$ was chosen. The assimilation frequency was set to 1 h since wave buoys typically have at least hourly measurements. From an operational and computational point of view, the assimilation frequency can be decreased, although this will decrease performance (illustrated in Section 8.

A sensitivity analysis of the initial settings was done and is presented in Section 8. In this identical twin experiment, five buoys displayed in green in Fig. 2 were used to assimilate synthetic hourly measurement. The buoy marked in yellow is used as an independent validation station to visualize typical time series and spectra. Since this is an identical twin experiment we have access to all hidden variables and thus validate performance over the entire spatio-temporal domain. With real data, validation can only be done with a limited number of observation stations.

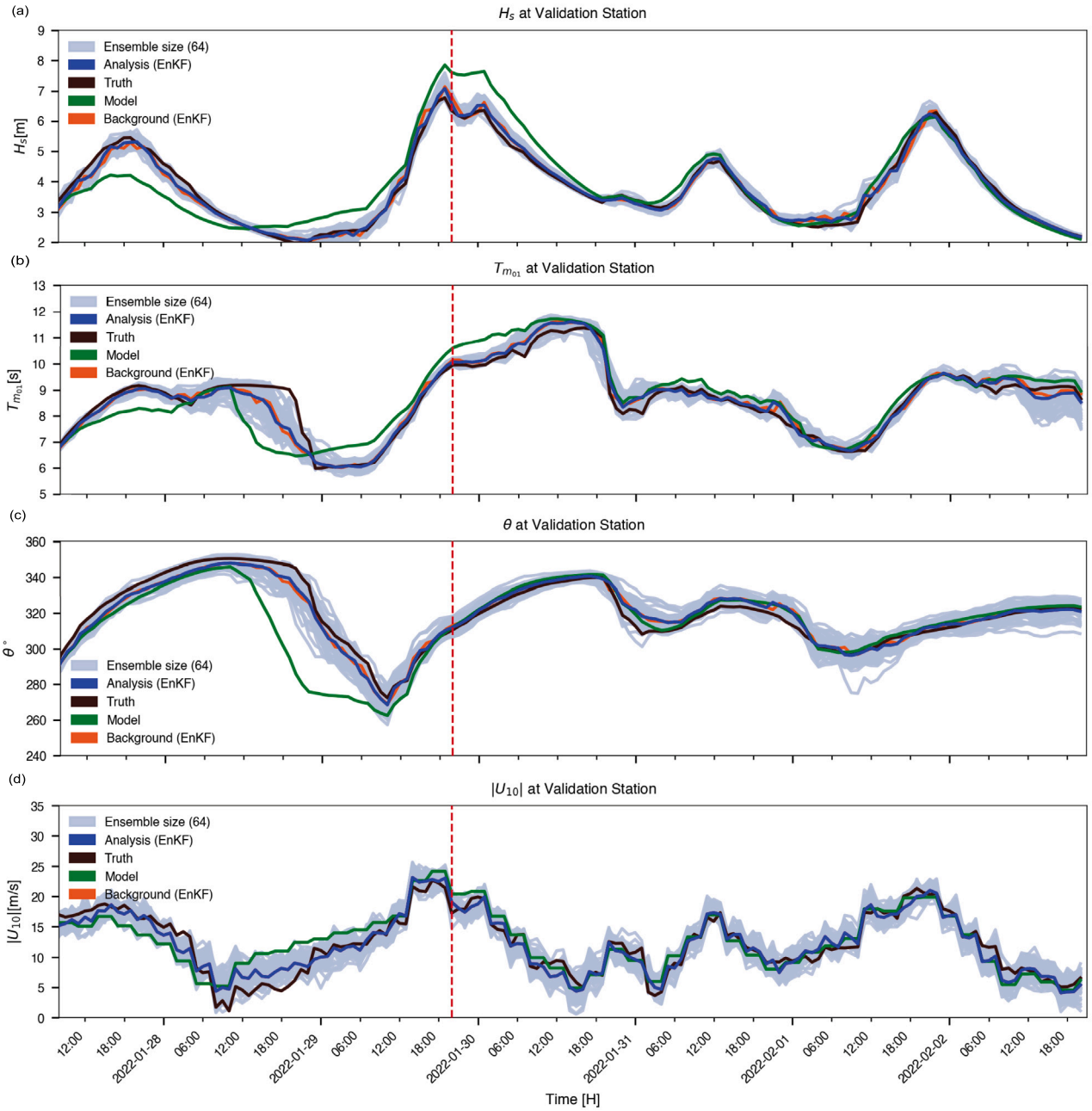

Fig. 3. Time series at the validation station showing the model free run (green), truth run (black), analysis (EnKF after correction) (blue) and background (EnKF before correction) (orange) for integral variables: (a) Significant wave height H_s; (b) Mean wave period T_{m01}; (c) Mean wave direction θ; (d) Wind speed at 10 m above surface $|U_{10}|$. The dashed red line represents the moment in time where the wave spectrum is shown in Fig. 4.

7.2. Physical consistency and performance

In this experiment, we assimilated H_s observations, but we also assessed the impact on other wave integral variables and wave spectra. If the EnKF performs well, spatio-temporal updates will display physical consistency and reduced errors. Additionally, a good representation of uncertainty requires the truth run to fall within the ensemble spread. Two particular questions of interest, when just assimilating H_s, are: (1) do the updates translate to other integral wave variables?; (2) are the updates confined to the area around the buoys? Note that in the identical twin context uncertainty statistics of the model and measurement are known.

To answer these questions, the time series of several integral variables are displayed in Fig. 3a,b,c and d displaying significant wave height H_s, mean wave period T_{m01}, mean wave direction θ and wind speed $|u_{10}|$ at the validation station. The analysis (blue) pulls closer towards the truth run (black) for H_s and notably for all integral variables, showcasing decreasing errors compared to the model free run (green). The truth run falls within the bounds of the ensemble spread, which means that uncertainty is represented correctly. The background (EnKF before correction) helps to visualize where strong updates are made. Not surprisingly, ensemble spread is typically larger for H_s during storm peaks where wind speeds reach their local maxima and because of the nonlinear relation between wind and wave growth. Interestingly, for mean wave period and direction, the ensemble spread is typically larger in a state of wind build-up (2022-01-28T12:00 to 2022-01-29T12:00) and rotating wind fields (2022-01-31T06:00 to 2022-01-31T14:00). This is likely to be associated with strong gradients in time and space. A snapshot of the rotating wind field is displayed in Fig. 2c.

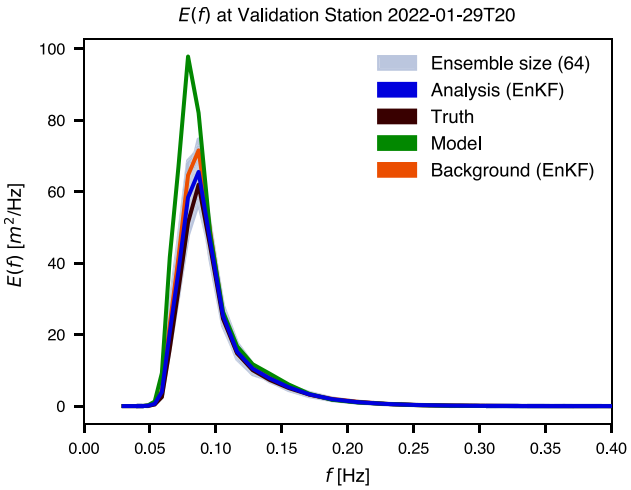

Fig. 4. 1D wave spectrum at 2022-01-29T20:00 with free run model, background (EnKF before correction) and analysis (EnKF after correction) and truth.

The fact that all integral variables – not just H_s – show improvements and a consistent ensemble, gives confidence that updates in the wind forcing translate well through the wave spectrum. To confirm this, a snapshot one-dimensional wave spectrum is displayed in Fig. 4. For a more straightforward visualization of the ensemble spread in Fig. 4, the one-dimensional instead of the two-dimensional spectrum was shown, but note that the directional bins are also updated. The corresponding moment in time for Fig. 4 is marked by a red dashed line in the time series panel in Fig. 3. Consistent updates between the one-dimensional spectrum and time series are displayed. The model free run (green) initially overestimated the wave energy and wave integral variables and the background (before update) and analysis (after update) converge towards the truth run (black). We can also observe a shift in peak energy from a lower frequency (model) to a higher frequency (EnKF), consistent with the mean wave period in Fig. 3.

After an illustration of physical consistency, the overall performance can be verified. Fig. 5a shows a scatter plot for the model free run result for variable H_s and Fig. 5b for the EnKF, including RMSE, scatter index (SI), bias and correlation coefficient R. The colour bar represents the relative likelihood of occurrence. The model scatter has some bi-modality that is caused by a clear separation of underestimation on the first day of the time series, while the model free run is mostly overestimating after the first day. It is difficult to draw any conclusions from this bi-modality, given that we have a short time window with very specific storm dynamics. RMSE score for H_s was reduced from 0.45 m to 0.16 m, SI from 0.13 to 0.05 and R was increased from 0.97 to 1.00. Bias remained the same. We cannot adhere strongly to the absolute values from this identical twin experiment, but the relative comparison between the model and EnKF is informative. For reference, Caires et al. (2018b) found reductions in a similar order assimilating real buoy data: SWAN driven by HARMONIE showed RMSE scores of 0.49–0.65 m, while the EnKF run reduced RMSE scores to 0.23–0.28 m.

The question that remains is whether updates are confined to the surroundings of the wave buoys or not. Fig. 6 shows that RMSE reductions up to 80 percent have been achieved throughout a large part of the North Sea, while the smallest reductions are found along the boundaries of the model. Most likely, a short wind fetch on the model edges limits the range of possible wind and wave updates.

Although good results were achieved with our initial settings derived from wind nowcast and forecast error estimates, one could question the validity and robustness of these settings when we do not have full knowledge of the system and measurement uncertainty statistics, e.g. when using real data. Next, we study the sensitivity of the initial settings

8. Results: EnKF sensitivity study

This Section is dedicated to understanding the sensitivity of the settings by using slightly different statistics in the EnKF compared to what we used to generate the synthetic truth and measurements. The EnKF is sensitive to: (a) the numerical settings of the filter; (b) the system uncertainty settings and (c) the measurement uncertainty settings. All sensitivity experiments are based on the twin experiment where observations from five synthetic wave buoys, displayed in Fig. 2a, were assimilated. To minimize the interaction between parameters during the sensitivity study, other parameters were kept constant. These values are displayed as grey dashed lines in Fig. 7.

8.1. Filter settings

Two important settings in the EnKF are the ensemble size and the assimilation frequency. Fig. 7a,b and c display sensitivity experiments for ensemble size, analysis frequency and computational speed for analysis frequency. Fig. 7a shows that the filter converges fully after ensemble size $N = 64$ (RMSE = 0.26 m). Although reasonable results can be achieved from $N = 16$ (RMSE = 0.28 m), statistics will be more prone to variance with a smaller ensemble size and slightly different case studies. The associated computational speed increases (not displayed here) exponentially with ensemble size from 15 ($N = 1$) min to 17 h ($N = 144$) with an hourly analysis frequency. For the rest of the experiments ensemble size 64 was used. Note that all grey vertical

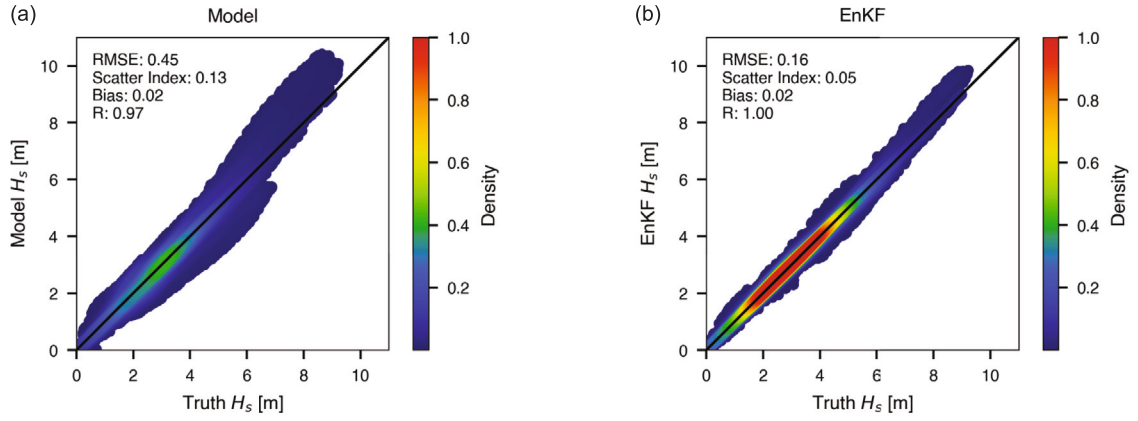

Fig. 5. Scatter plots for predicted H_s and true H_s: (a) results for the model free run; (b) results for the EnKF buoy observation assimilation. The colour bar shows the relative likelihood of pairs to occur.

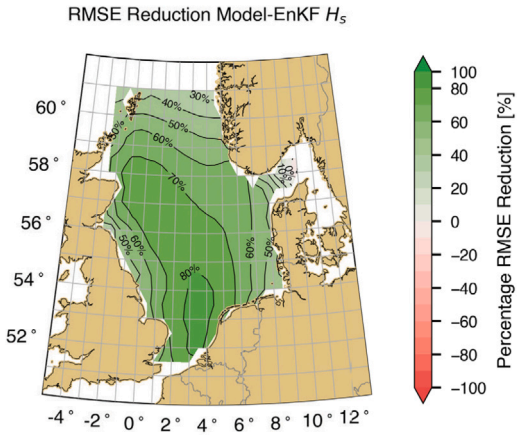

Fig. 6. Percentage of RMSE reduction between model and EnKF for H_s averaged over time. Positive percentages indicate a reduction in RMSE for the EnKF.

dashed lines in Fig. 7 display the settings that were kept constant in the other experiments.

The filter is also sensitive to how often observations are assimilated: the analysis or assimilation frequency. This is relevant when observations are not available at regular intervals (satellite observations). There is a trade-off between performance and computational speed. This becomes evident when comparing the nonlinear increase of the RMSE in Fig. 7b and the associated computational speed in Fig. 7c. The best performance occurs when hourly observations are assimilated, but computational speed decreases rapidly for a frequency of 6 h, while still maintaining acceptable performance. An assimilation frequency of 6 h was used for the rest of the experiments, anticipating the satellite altimeter twin experiment. Changing the assimilation frequency to 1 h did not change the results significantly.

8.2. Observation uncertainty settings

Fig. 7d shows RMSE scores for the availability of observations. It shows that there is little benefit in assimilating hourly observations when the assimilation frequency is 6 h (even a RMSE increase from 0.27 m compared to 0.3 m). RMSE scores increase nonlinearly to a lower availability of 21 h. Given the short simulation time window, the observation samples become too small after 21 h. Fig. 7e displays the sensitivity to observation uncertainty while keeping the standard deviation of the observation noise of the synthetic observations constant. It is obvious that underestimating the observation noise is penalized more than overestimating it, with exponentially increasing RMSE scores. Although the optimal standard deviation was found to be 0.3 m, slightly higher compared to the actual noise standard deviation on synthetic observations (0.2 m). This could be caused by two things. A compensation effect due to a limited ensemble size and the 6-h assimilation frequency, to maintain sufficient ensemble spread.

8.3. System uncertainty settings

Recall that we chose initial settings based on the nowcast and forecast HARMONIE wind fields. Fig. 7f,g and h show low sensitivity to wind correlation length and time scale as well as uncertainty. Fig. 7f,g and h display that the optimal values slightly shift, compared to the settings to generate the synthetic truth (grey dashed lines), when using a 6-hourly assimilation frequency. In contrast, the ensemble spread was slightly less optimal for the lowest RMSE scores. Therefore, the initial settings consistent with the truth run settings were not changed.

9. Results: assimilation synthetic altimetry observations

9.1. Synthetic satellite altimeter measurements

This Section evaluates the potential impact of satellite altimeter measurements in an EnKF wave DA system for the North Sea. This also allows for a relative comparison between the impact of assimilating buoy and satellite altimeter measurements. In this experiment, synthetic H_s observations from satellite altimeters were assimilated, using the actual spatial coverage and pass-over times. This comparison is of interest because buoy measurements are typically abundant in time, but scarce in space, while satellite altimeter measurements are typically scarce in time and abundant in space. All available satellite observations of H_s were used and include satellites: nadir CFOSAT, Haiyang-2B, Cryosat −2, Jason-3, Sentinel-3, Saral and Altika. They were obtained from the Copernicus Marine Environment Monitoring Service (CMEMS) Data Store. Fig. 8 shows a typical day (2022-01-31) of satellite altimeter tracks that provide H_s observations in colour, and all tracks over the simulation period in grey.

It must be noted that one Sentinel-3B track was not available on CMEMS. Moreover, Altika and Saral did not cross the North Sea on this date. The average time between tracks is approximately 4 h, but the maximum gap between tracks is 12 h. Occasionally 2 tracks within one hour occur. The synthetic H_s measurements for satellite tracks were created by extracting them from the perturbed truth model run and perturbed with white noise with a standard deviation of 0.2 m, which is approximately equal to the error statistics that CMEMS provides for the wave altimeter product (Taburet et al., 2024). Although there are small variations between satellite altimeters, the standard deviation was kept constant for consistency of the identical twin experiments. To avoid overloading the system with observations, while using a coarse grid, sufficient spacing between points on the track was taken (every 10th point). A coastal mask of 50 km was applied to be consistent with the decreased performance of altimeter tracks nearshore.

9.2. Physical consistency: Haiyang-2B snapshot

To verify the behaviour of the EnKF using satellite altimeter measurements and the physical consistency in the system, this Section shows a detailed comparison of the corrections in time and space. Fig. 9 shows a time series at validation station Anasuria. The SWAN model free run is displayed in green, the synthetic truth in black, the background (before correction) in orange and the analysis (EnKF after correction) in blue. The dashed lines indicate when satellite observations were assimilated, with the red dashed line representing the pass-over of Haiyang-2B satellite track on 2022-01-31 07:00.

First of all the EnKF analysis (blue) is closer to the truth (black) compared to the model (green) and EnKF background (orange), showcasing a good performance of the EnKF. Secondly, the ensemble spread varies over time, underlining the dynamic state-dependent uncertainty in the system similar to our buoy experiment.

The difference here is that the ensemble spread grows larger compared to the buoy experiment, caused by the decreased temporal availability of satellite measurements. This holds in particular when wind speeds are high. The ensemble spread during the time interval between 2022-01-31 17:00 and 2022-02-01 09:00 clearly shows this. Thirdly, by comparing the background (before correction) with the analysis (after correction) on the analysis intervals, the impact of the EnKF becomes apparent. The pass-over of Haiyang-2B on 2022-01-31 07:00 is particularly interesting because the system has not received an observation for a longer period and encountered growing uncertainty. The dashed line marks a decrease in H_s after the correction. Also, the ensemble spread decreases as a result of the updated information in the system (and possibly the decaying wind speed).

Although the time series indicate good corrections on H_s, the wave spectrum could provide more convincing evidence for physically

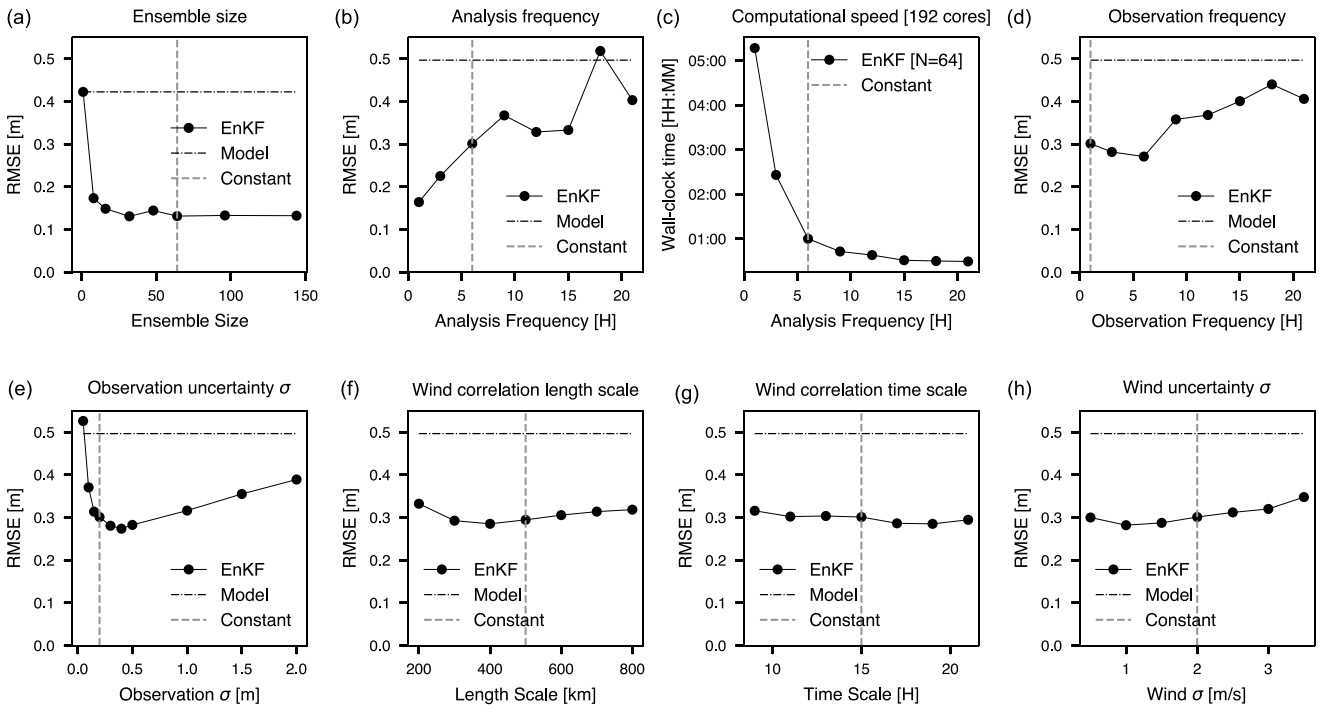

Fig. 7. Sensitivity experiments for the EnKF Wave DA system. Sensitivity for (a) ensemble size; (b) analysis frequency; (c) computational speed for analysis frequency; (d) observation frequency; (e) observation uncertainty; (f) wind correlation length scale; g) wind correlation length scale (h); standard deviation of the wind forcing noise. Dashed lines indicate settings kept constant.

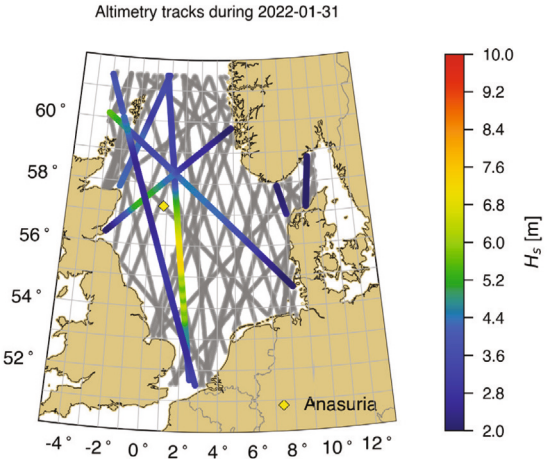

Fig. 8. Observed daily altimeter tracks for 2022-01-31 (colour) and remaining tracks (grey) including nadir CFOSAT, Haiyang-2B, Cryosat −2, Jason-3, Sentinel-3.

consistent and realistic corrections. After all, corrections are made through covariance between the wind fields and the wave spectrum. Fig. 10 shows the model free run one-dimensional wave spectrum, the background EnKF (before correction) and the analysis EnKF (after correction). A consistent correction is made on the wave spectrum, decreasing the energy in the peak of the spectrum that was overestimated as a result of uncertainty in the wind field. It is worth noting that we occasionally found wave spectra where the low-frequency energy was increased, while the wind speed was decreased. This could occur when wind speed drops and correlates with the low-frequency part of the wave spectrum, which can be physically consistent.

To illustrate the wave DA system with satellite altimeter measurements, spatial patterns of the wind and wave fields and the respective corrections are analysed. Fig. 11 displays 6 panels. The first row displays the background wind field (U_{10}) at 2022-01-31 07:00, the correction on the wind field after assimilating Haiyang-2B and the error reduction of U_{10} after the analysis. The second row in the panel displays the same metrics, but instead for the wave field (H_s). Additionally, Fig. 11d also marks the Haiyang-2B (H2b) observations. 11e displays the innovation (observed-background) at the satellite track points. Fig. 11e and f show the location of validation station Anasuria. The sharp gradient in the wind and wave fields makes this an interesting moment in time. Panels 11b and e clearly display both positive and negative updates for U_{10} and H_s. This can be explained by the difference in the covariance structure of strong winds in the western North Sea and weaker (rotated) winds in the eastern North Sea. Improved error reduction scores are shown (in blue) in the third column for both wind and waves, although the extent of improvement is larger for the wave field. This is to be expected, knowing that wind fields are corrected to be consistent with wave fields. The southwestern North Sea performs slightly worse. This could be caused by the use of a uniform correlation length scale and the absence of observations in the southwestern part of the North Sea.

9.3. Overall spatial performance

After an illustration of the physical consistency of the wave DA system, the overall performance metrics can be assessed in terms of the respective distributions and errors in space and time. Fig. 12 shows the percentage of RMSE reduction between the model and EnKF for H_s averaged over time. Although, less widespread compared to the hourly buoy assimilation, RMSE reductions of up to 60 percent are achieved. The decreased observation availability impacts the southwestern part of the North Sea most, similarly as visible in the snapshot in Fig. 11f. Most likely, hourly buoy measurements covering the entire North Sea extent, can partly compensate for the simplified uniform correlation length scale of the wind noise model. However, when the satellite tracks do not extend across the meridional extent of the North Sea, the EnKF (unfavourably) relies more on the uniform correlation length scale.

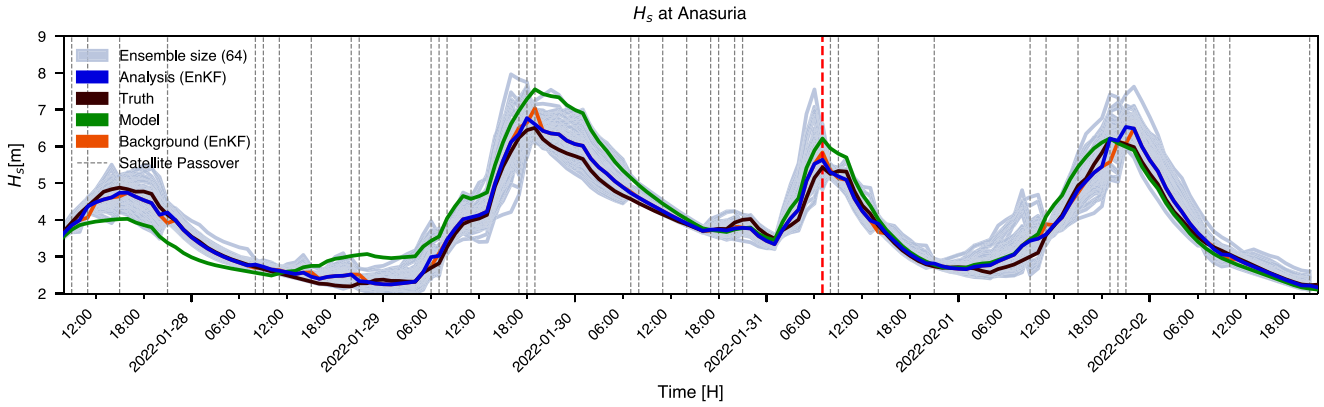

Fig. 9. Time series at validation station Anasuria displaying the ensemble spread (grey), the analysis (EnKF after correction) (blue), the background (EnKF before correction) (orange), the free run model (green), the synthetic truth (black), all satellite pass-over times and the Haiyang-2B pass-over time (also displayed in Fig. 11).

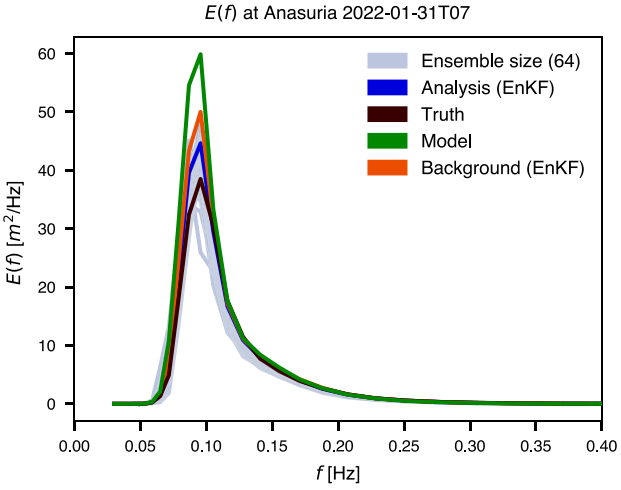

Fig. 10. 1D wave spectrum at 2022-01-31T07:00:00 with free run model, background (EnKF before correction), analysis (EnKF after correction) and truth.

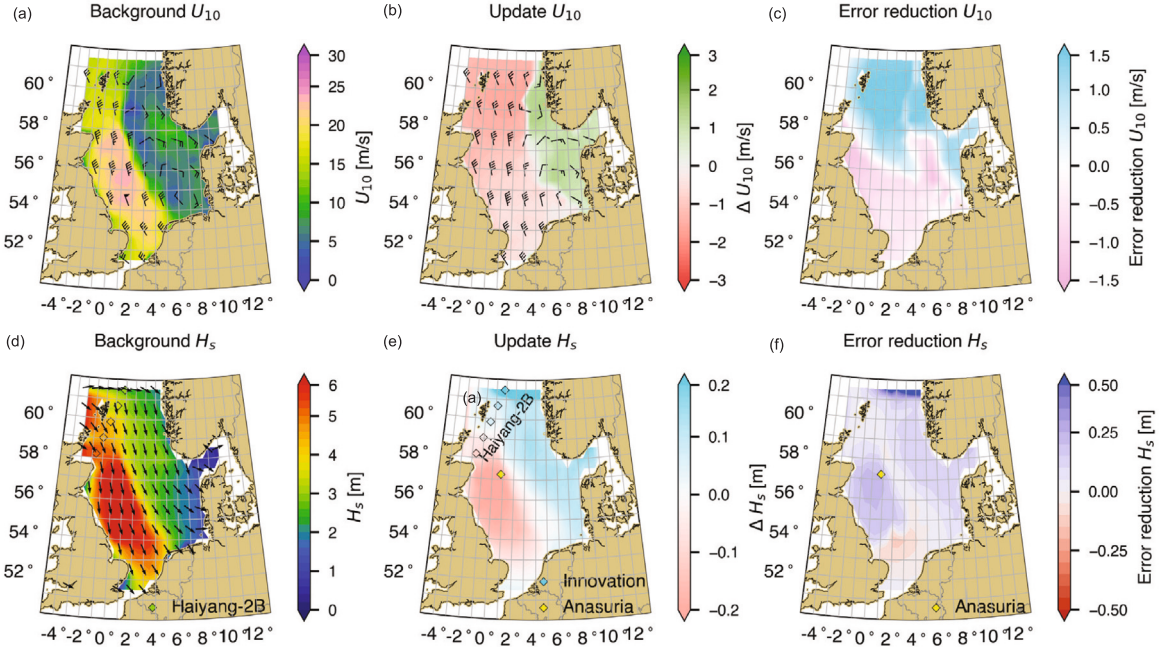

Fig. 11. Spatial fields at 2022-01-31T07:00:00 with (a) EnKF background U_{10} [m/s]; (b) U_{10} EnkF update (analysis-background) [m/s]; (c) U_{10} Error reduction compared to background [m]; (d) EnKF background H_s [m] and Haiyang-2B satellite observations; (e) H_s EnKF update and the innovation (observed-background) for Haiyang-2B track; (f) H_s Error reduction compared to background [m].

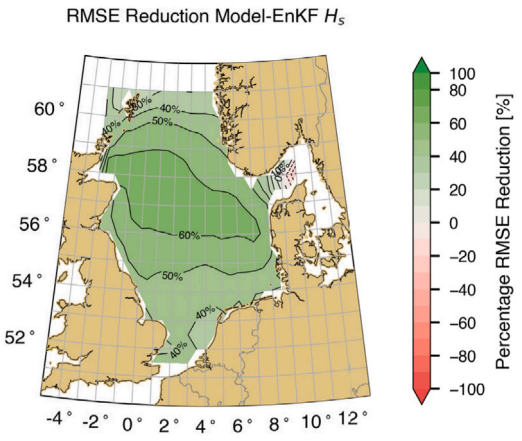

Fig. 12. Percentage of RMSE reduction between model and EnKF for H_s averaged over time. Positive percentages indicate a reduction in RMSE for the EnKF.

9.4. Overall time performance

Fig. 13 shows a scatter plot of truth and predicted H_s for both the EnKF and the model free run, including performance metrics for all grid cells and the entire time series. The density on the colour bar shows the relative likelihood of the distributions. The EnKF shows improved performance reducing the RMSE from 0.44 to 0.21 and scatter index from 0.13 to 0.06. Bias reverses from 0.02 to −0.03, but it should be taken into account that we assessed a limited time period.

To illustrate the co-dependence of the error and uncertainty on the information availability in the system, Fig. 14 shows that ensemble spread and RMSE grow, when satellite observations are absent for a longer period, indicated by the dashed lines. The time windows, where this is not the case, e.g. 2022-02-01 11:00 and 19:00 can be explained by the fact that the satellite track just crosses a small tip of the model domain, allowing the error to grow because of limited observations.

10. Discussion

The buoy experiment (RMSE = 0.16 m) relatively outperforms the satellite experiment (RMSE = 0.21 m) and strong RMSE reductions are more widespread throughout the North Sea. The time between satellite passes sometimes shows larger gaps, and errors can grow significantly if this coincides with increasing strong winds and waves. In contrast, buoys have a very regular sampling, but there are several parts of the North Sea with few buoys (although there are more platforms and buoys than used in this study). In space and time, both experiments have physically consistent corrections, that are to some extent confined by the surroundings of the measurements.

The RMSE averaged over the model domain shows the reduced impact of irregular measurement sampling when comparing satellite and buoy results. Despite this, the study shows that the impact of assimilating satellite altimeter measurements can be significant. Identical twin results cannot support strong conclusions in relation to real data. Still results from Caires et al. (2018a) are in the same order of magnitude of 10–30 cm in an experiment where buoy H_s observations were assimilated. Ensemble size, observation frequency, observation uncertainty, and analysis frequency are relatively important settings to consider in the EnKF. The parameters for the noise model to perturb the wind fields are less sensitive. There is some interaction between parameters while changing the analysis frequency, but this does not significantly change the outcome. Note that we considered a specific storm within a short time window, so some variance in results can be expected under different physical conditions and a longer simulation period. Another limitation is that we used a relatively coarse resolution for our model domain and inputs.

Putting the results in a broader perspective, several promising research opportunities arise. Firstly, an observation impact study would allow us to test this framework with real satellite data.

Secondly, the recent launch of the SWOT satellite mission (Surface Water Ocean Topography) opens up several ways of looking at H_s spatial variability (Bohé et al., 2025). The instrument measures over a wide swath of 120 km with a 20 km gap in the middle (Fu et al., 2024). Moreover, this adds one extra satellite, increasing the temporal density.

Due to the nature of satellite altimeter wave measurements, only measurements of H_s were assimilated. Nonetheless, the EnKF implementation is suitable for the assimilation of various other variables. Investigating the potential of assimilating wind measurements (e.g. from scatterometer) is an interesting opportunity for future research.

11. Conclusion

We implemented a wave DA system based on the EnKF, illustrating advantages over existing schemes with identical twin experiments. By using the full wave spectra in the state and just assimilating integral variable H_s, physically consistent correction on the wave spectrum and other integral variables are achieved. A sensitivity study shows the relative importance of observation frequency, knowledge of observation uncertainty, ensemble size and assimilation frequency. In contrast, the noise model parameters are less sensitive. The satellite experiment (0.44 to 0.21 RMSE reduction) performs slightly worse than the buoy experiment (0.45 m to 0.16 m RMSE reduction), due to

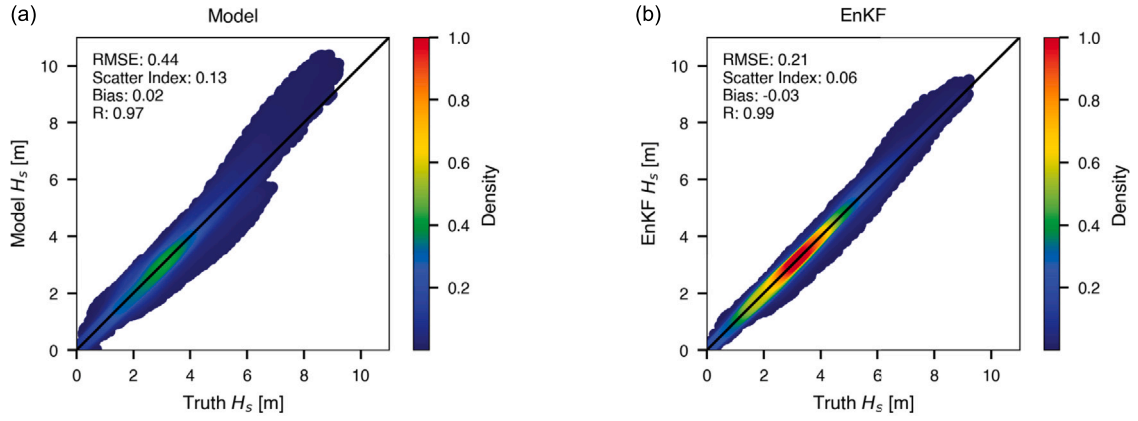

Fig. 13. Scatter plots for predicted H_s and true H_s: (a) results for the model free run; (b) results for the EnKF satellite assimilation. The colour bar shows the relative likelihood of pairs to occur.

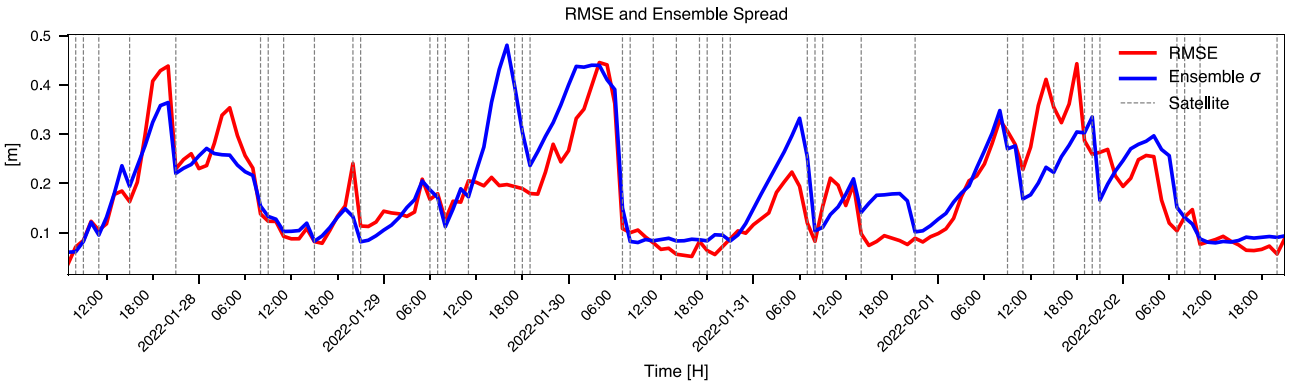

Fig. 14. Time series of the H_s RMSE, averaged over the model domain, the ensemble spread and the pass-over times of the assimilated satellite observations.

reduced observation availability and varying spatial coverage. Despite this, such a system provides a promising framework for observation impact studies. A good improvement over existing schemes is that the assimilation impact is not affected by ad-hoc choices for converting changes in H_s to updates of the full wave spectra. The experiments indicate that the potential impact of satellite H_s measurements in the North Sea can be significant and worth further exploration. Although the error structure and settings are realistic, one should still be careful about extrapolation to experiments with real measurements.

CRediT authorship contribution statement

C.W.E. de Korte: Writing – original draft, Visualization, Software, Methodology, Investigation, Formal analysis, Conceptualization. **M. Verlaan:** Writing – review & editing, Supervision, Software, Methodology, Conceptualization. **A.W. Heemink:** Writing – review & editing, Supervision, Methodology, Conceptualization.

Declaration of competing interest

The authors declare that they have no known competing financial interests or personal relationships that could have appeared to influence the work reported in this paper.

Acknowledgements

This research was supported by Deltares, Netherlands. This work used the Dutch national e-infrastructure with the support of the SURF Cooperative using grant no. EINF-7464. We are grateful for feedback from Caroline Gautier and Björn Backeberg who reviewed the first article draft. We also thank Julius Sumihar and Nils van Velzen for their technical software support.

Appendix A. Cholesky factorization

In the actual implementation of the EnKF scheme, the computation of covariance matrices (Eqs. (9) and (14)) can be avoided. More specifically, we take the Cholesky factorization (Lewis et al., 2006, 9.1) of real symmetric positive and definite matrix $\mathbf{P}^f(t_k)$ as

$$\mathbf{P}^f(t_k) = \mathbf{L}(t_k)\mathbf{L}^T(t_k), \tag{A.1}$$

where $\mathbf{L}$ is the perturbation matrix of size nxN, with n being the number of state variables and N the ensemble size:

$$\mathbf{L}(t_k) = \frac{1}{\sqrt{N-1}}\left[\xi_i^f(t_k) - \hat{\mathbf{x}}^f(t_k),\ \ldots,\ \xi_N^f(t_k) - \hat{\mathbf{x}}^f(t_k)\right] \tag{A.2}$$

We can map the perturbation matrix to the observations to reduce dimensions by taking

$$\mathbf{\Psi}(t_k) = \mathbf{H}\mathbf{L}^f(t_k) \tag{A.3}$$

with dimensions of $\Psi(t_k)$ being mxN where m is the number of observations and n the number of state variables. By means of substitution using Eqs. (A.1) and (A.3), the Kalman gain can be reformulated as:

$$\mathbf{K}(t_k) = \mathbf{L}(t_k)\mathbf{\Psi}^T(t_k)\left[\mathbf{\Psi}(t_k)\mathbf{\Psi}^T(t_k) + \mathbf{R}(t_k)\right]^{-1} \tag{A.4}$$

Appendix B. Non-linear observation operator

In the EnKF formulation, the measurement operator $\mathbf{H}$ is assumed linear. However, the wave measurements are often in H_s [m] and the wave model state in $E(\sigma,\theta)$ [m^2/Hz], so a nonlinear operation is needed. We use a similar concept as in Hunt et al. (2007) and apply H to each ensemble member and the ensemble mean separately. To this end $\mathbf{\Psi}$ can be defined as:

$$\mathbf{\Psi}(t_k) = \frac{1}{\sqrt{N-1}}\left[H(\xi_i^f(t_k)) - H(\hat{\mathbf{x}}^f(t_k))\right]_{i=1}^{N} \tag{B.1}$$

It is obvious that this holds with a linear measurement operator, but it is also a reasonable approximation for a nonlinear measurement operator when deviations around the mean are small. Thus we can replace Eq. (A.3) with Eq. (B.1). Consequently, Eqs. (A.2) and (A.4) contain the transformed ensemble predictions of the observations.

Data availability

The open source data assimilation software, OpenDA, can be downloaded from: https://github.com/OpenDA-Association. The wave model SWAN can be downloaded from: https://gitlab.tudelft.nl/citg/wavemodels/swan. Satellite altimeter tracks used to create synthetic data are accessible through the Copernicus Marine Environment Monitoring Service (CMEMS): https://doi.org/10.48670/moi-00179.

References

Almeida, S., Rusu, L., Guedes Soares, C., 2016. Data assimilation with the ensemble Kalman filter in a high-resolution wave forecasting model for coastal areas. J. Oper. Ocean. 9 (2), 103–114.

Aouf, L., Lefèvre, J.-M., Hauser, D., 2006. Assimilation of directional wave spectra in the wave model WAM: An impact study from synthetic observations in preparation for the SWIMSAT satellite mission. J. Atmos. Ocean. Technol. 23 (3), 448–463.

Bohé, A., Chen, A., Chen, C., Dubois, P., Fore, A., Molero, B., Peral, E., Raynal, M., Stiles, B., Ardhuin, F., et al., 2025. Measuring significant wave height fields in two dimensions at kilometric scales with swot.. IEEE Trans. Geosci. Remote Sens..

Booij, N., Ris, R.C., Holthuijsen, L.H., 1999. A third-generation wave model for coastal regions: 1. Model description and validation. J. Geophys. Res.: Ocean. 104 (C4), 7649–7666.

Burgers, G., Van Leeuwen, P.J., Evensen, G., 1998. Analysis scheme in the ensemble Kalman filter. Mon. Weather Rev. 126 (6), 1719–1724.

Caires, S., Kim, J., Groeneweg, J., 2018a. Korean East Coast wave predictions by means of ensemble Kalman filter data assimilation. Ocean. Dyn. 68 (11), 1571–1592.

Caires, S., Marseille, G., Verlaan, M., Stoffelen, A., 2018b. North sea wave analysis using data assimilation and mesoscale model forcing winds. J. Waterw. Port, Coast. Ocean. Eng. 144 (4), 04018005.

Cavaleri, L., Abdalla, S., Benetazzo, A., Bertotti, L., Bidlot, J.-R., Breivik, Ø., Carniel, S., Jensen, R.E., Portilla-Yandun, J., Rogers, W.E., et al., 2018. Wave modelling in coastal and inner seas. Prog. Oceanogr. 167, 164–233.

De Las Heras, M.M., Burgers, G., Janssen, P.A., 1994. Variational wave data assimilation in a third-generation wave model. J. Atmos. Ocean. Technol. 11 (5), 1350–1369.

Esteva, D.C., 1988. Evaluation of preliminary experiments assimilating seasat significant wave heights into a spectral wave model. J. Geophys. Res.: Ocean. 93 (C11), 14099–14105.

Evensen, G., 1994. Sequential data assimilation with a nonlinear quasi-geostrophic model using Monte Carlo methods to forecast error statistics. J. Geophys. Res.: Ocean. 99 (C5), 10143–10162.

Evensen, G., 2004. Sampling strategies and square root analysis schemes for the enkf. Ocean. Dyn. 54, 539–560.

Fu, L.-L., Pavelsky, T., Cretaux, J.-F., Morrow, R., Farrar, J.T., Vaze, P., Sengenes, P., Vinogradova-Shiffer, N., Sylvestre-Baron, A., Picot, N., et al., 2024. The surface water and ocean topography mission: A breakthrough in radar remote sensing of the ocean and land surface water. Geophys. Res. Lett. 51 (4), e2023GL107652.

Gautier, C., Caires, S., 2015. Operational wave forecasts in the southern north sea. In: 36th IAHR World Congress, 28th June–3 July. Vol. 1, p. 5.

Hasselmann, K., Barnett, T.P., Bouws, E., Carlson, H., Cartwright, D.E., Enke, K., Ewing, J., Gienapp, A., Hasselmann, D., Kruseman, P., et al., 1973. Measurements of wind-wave growth and swell decay during the joint north sea wave project (JONSWAP).. Ergaenzungsheft Zur Dtsch. Hydrogr. Z. Reihe A.

Hasselmann, S., Lionello, P., Hasselmann, K., 1997. An optimal interpolation scheme for the assimilation of spectral wave data. J. Geophys. Res.: Ocean. 102 (C7), 15823–15836.

Houghton, I.A., Hegermiller, C., Teicheira, C., Smit, P.B., 2022. Operational assimilation of spectral wave data from the sofar spotter network. Geophys. Res. Lett. 49 (15), e2022GL098973.

Houghton, I.A., Penny, S.G., Hegermiller, C., Cesaretti, M., Teicheira, C., Smit, P.B., 2023. Ensemble-based data assimilation of significant wave height from sofar spotters and satellite altimeters with a global operational wave model. Ocean. Model. 183, 102200.

Hunt, B.R., Kostelich, E.J., Szunyogh, I., 2007. Efficient data assimilation for spatiotemporal chaos: A local ensemble transform Kalman filter. Phys. D: Nonlinear Phenom. 230 (1–2), 112–126.

Janssen, P.A., Lionello, P., Reistad, M., Hollingsworth, A., 1989. Hindcasts and data assimilation studies with the WAM model during the seasat period. J. Geophys. Res.: Ocean. 94 (C1), 973–993.

Kalman, R.E., 1960. A new approach to linear filtering and prediction problems.

Kim, J., Yoo, J., Do, K., 2020. Wave data assimilation to modify wind forcing using an ensemble Kalman filter. Ocean. Sci. J. 55, 231–247.

Komen, G., 1994. Dynamics and modelling of ocean waves. Dyn. Atmosphere Ocean. 25 (4), 276.

Komen, G., Hasselmann, S., Hasselmann, K., 1984. On the existence of a fully developed wind-sea spectrum. J. Phys. Oceanogr. 14, 1271–1285.

Lam, R., Sanchez-Gonzalez, A., Willson, M., Wirnsberger, P., Fortunato, M., Alet, F., Ravuri, S., Ewalds, T., Eaton-Rosen, Z., Hu, W., et al., 2022. GraphCast: Learning skillful medium-range global weather forecasting. arXiv preprint arXiv:2212.12794.

Lang, S., Alexe, M., Chantry, M., Dramsch, J., Pinault, F., Raoult, B., Clare, M.C., Lessig, C., Maier-Gerber, M., Magnusson, L., et al., 2024. AIFS-ECMWF's data-driven forecasting system. arXiv preprint arXiv:2406.01465.

Lewis, J.M., Lakshmivarahan, S., Dhall, S., 2006. Dynamic Data Assimilation: a Least Squares Approach. Vol. 13, Cambridge University Press.

Li, J., Zhang, S., 2020. Mitigation of model bias influences on wave data assimilation with multiple assimilation systems using WaveWatch III v5. 16 and SWAN v41. 20. Geosci. Model. Dev. 13 (3), 1035–1054.

Lionello, P., Günther, H., Hansen, B., 1995. A sequential assimilation scheme applied to global wave analysis and prediction. J. Mar. Syst. 6 (1–2), 87–107.

Ribal, A., Young, I.R., 2019. 33 years of globally calibrated wave height and wind speed data based on altimeter observations. Sci. Data 6 (1), 77.

Ridler, M.E., van Velzen, N., Hummel, S., Sandholt, I., Falk, A.K., Heemink, A., Madsen, H., 2014. Data assimilation framework: Linking an open data assimilation library (openda) to a widely adopted model interface (openmi). Environ. Model. Softw. 57, 76–89.

Sakov, P., Evensen, G., Bertino, L., 2010. Asynchronous data assimilation with the enkf. Tellus A: Dyn. Meteorol. Ocean. 62 (1), 24–29.

Saulter, A.N., Bunney, C., King, R.R., Waters, J., 2020. An application of NEMOVAR for regional wave model data assimilation. Front. Mar. Sci. 7, 579834.

Schlembach, F., Ehlers, F., Kleinherenbrink, M., Passaro, M., Dettmering, D., Seitz, F., Slobbe, C., 2023. Benefits of fully focused SAR altimetry to coastal wave height estimates: A case study in the north sea. Remote Sens. Environ. 289, 113517.

Skandrani, C., Lefevre, J.-M., Queffeulou, P., 2004. Impact of multisatellite altimeter data assimilation on wave analysis and forecast. Mar. Geod. 27 (3–4), 511–533.

Smit, P., Houghton, I., Jordanova, K., Portwood, T., Shapiro, E., Clark, D., Sosa, M., Janssen, T., 2021. Assimilation of significant wave height from distributed ocean wave sensors. Ocean. Model. 159, 101738.

Song, Q., Mayerle, R., 2017. A 4D variational assimilation scheme with partition method for nearshore wave models. Ocean. Dyn. 67 (8), 989–1002.

Taburet, N., Husson, R., Charles, E., Jettou, G., Philip, A., Philipps, S., Ghantous, M., Kocha, C., 2024. WAVE thematic assembly centre: Wave_glo_phy_ swh_l3_nrt _014_001.

Tourain, C., Piras, F., Ollivier, A., Hauser, D., Poisson, J.-C., Boy, F., Thibaut, P., Hermozo, L., Tison, C., 2021. Benefits of the adaptive algorithm for retracking altimeter nadir echoes: Results from simulations and CFOSAT/SWIM observations. IEEE Trans. Geosci. Remote Sens. 59 (12), 9927–9940.

Voorrips, A., Heemink, A., Komen, G., 1999. Wave data assimilation with the Kalman filter. J. Mar. Syst. 19 (4), 267–291.

Voorrips, A., Makin, V., Hasselmann, S., 1997. Assimilation of wave spectra from pitch-and-roll buoys in a north sea wave model. J. Geophys. Res.: Ocean. 102 (C3), 5829–5849.

Wang, C., Li, S., Yu, H., Wu, K., Lang, S., Xu, Y., 2024. Comparison of wave spectrum assimilation and significant wave height assimilation based on Chinese-french oceanography satellite observations. Remote Sens. Environ. 305, 114085.

Yu, H., Li, J., Wu, K., Wang, Z., Yu, H., Zhang, S., Hou, Y., Kelly, R.M., 2018. A global high-resolution ocean wave model improved by assimilating the satellite altimeter significant wave height. Int. J. Appl. Earth Obs. Geoinf. 70, 43–50.

Zijderveld, A., Verlaan, M., 2004. Towards a new gridded bathymetry for storm surge forecasting in the north sea. In: Geophysical Research Abstracts. Vol. 6, p. 05177.

Zijl, F., Zijlker, T., Laan, S., et al., 2022. 3D DCSM FM: A Sixth-Generation Model for The NW European Shelf. Technical Report, Deltares.